Scanning Electron Microscopy

Volume 1985
Number 2 *Part II*

Article 6

5-15-1985

Progress in High Resolution Scanning Ion Microscopy and Secondary Ion Mass Spectrometry Imaging Microanalysis

R. Levi-Setti
The University of Chicago

G. Crow
The University of Chicago

Y. L. Wang
The University of Chicago

SCANNING ELECTRON MICROSCOPY/1985/II (Pages 535-551)
SEM Inc., AMF O'Hare (Chicago), IL 60666 USA

0586-5581/85$1.00+.05

PROGRESS IN HIGH RESOLUTION SCANNING ION MICROSCOPY AND SECONDARY ION MASS SPECTROMETRY IMAGING MICROANALYSIS

R. Levi-Setti,* G. Crow and Y.L. Wang

The Enrico Fermi Institute and Department of Physics
The University of Chicago, Chicago, Illinois 60637

(Paper received April 2 1985, Completed manuscript received May 15 1985)

Abstract

The performance of a new high resolution scanning ion microprobe (SIM) is elucidated with regard to imaging capabilities using the ion-induced secondary electron (ISE) or secondary ion (ISI) signals, and the mass-resolved signal from a secondary ion mass spectrometry (SIMS) system. The new instrument focuses a beam extracted from a liquid metal ion source (LMIS) to a range of spot sizes reaching the 20 nm level. The probe current (1.6 pA) available at this level of lateral resolution, which approaches the theoretical resolution limits of the SIMS method, is still adequate to obtain detailed isotopic maps for surfaces rich in the elements of low ionization potential (positive ISI), or high electron affinity (negative ISI). In addition to examples of high resolution ISE and ISI images of objects displaying sufficiently small topographic detail, mass spectra and isotopic maps are shown, testing both the lateral and depth resolution attained. The latter results belong with a program of interdisciplinary research applications of the new microprobe, which include studies of e.g., the monolayer lateral distribution of intercalant in $SbCl_5$ intercalated graphite and of silicate minerals and iron distribution in sections of chondrules and their rims (components of chondrites, a class of stoney meteorites). In the biomedical field, the new microprobe finds application in e.g., the study of human renal calculi and bone. Most promising is the use of stable isotope tracers (e.g., Ca^{44}) to unravel the dynamics of bone mineralization, as thus far shown with the in-vitro culture of the skull bone of neonatal mice.

Keywords: Liquid metal ion sources, scanning ion microscopy, secondary ion mass spectrometry (SIMS), imaging microanalysis, imaging SIMS, gallium and indium focused ion probes, high spatial resolution, isotopic maps, stable isotope labeling, secondary electron and secondary ion emission.

*For reprints and other information contact R. Levi-Setti at the above address. Phone No.: (312) 962-7827.

Introduction

The attainment of high spatial resolution in images obtained using destructive probes such as those extracted from liquid metal ion sources (LMIS) in a scanning ion microprobe (SIM), requires careful optimization of many parameters affecting both the target sample and its retrieved image. This holds true in either the imaging of the surface topography exploiting the *ion*-induced *secondary electron* (ISE) or *ion* (ISI) signals (Levi-Setti, 1983), or in the mapping of the isotopic surface distribution using the mass-resolved signal from a secondary ion mass spectrometry (SIMS) system. A small probe size is by no means synonymous with high spatial image resolution, unless relevant aspects of the probe-target interaction and of the image acquisition system are taken into account. Clearly, to reduce the loss of surface detail resulting from depth-averaging or lateral smoothing due to sample erosion during ISE or ISI image acquisition, the total primary ion dose should be maintained at a practical minimum. This condition is even more stringent in SIMS imaging, where one wishes to restrict the sampled depth to the intrinsic ISI escape depths, typically comparable to the thickness of one monolayer. This requirement will translate, for a given probe current, to limits on the imaged sample area or image magnification. Concurrent requirements for high resolution SIMS imaging involve consideration of the optimum specimen sampling with a digital raster, of the time of flight of the mass-analyzed ions, and of the conditions required to maintain adequate oxygen coverage of the sample to enhance ISI yields. These have been discussed previously (Levi-Setti, et al., 1984a) and will be reexamined in the context of this report.

An overall scaling factor, which may allow or deny the matching of the probe size with image resolution in SIM or SIMS imaging, is represented by the collection efficiency for the ISE or ISI signals, and by the overall transmission of the SIMS system. With carefully designed SIM and SIMS systems, coupled to a high resolution image display, it has been feasible to preserve the matching of beam spot size and image resolution to reach the 20 nm level in both ISE, ISI or SIMS images, with probe currents as low as 1 pA, thus reducing the surface sample consumption to a fraction of a monolayer when the dwell time per pixel is $\lesssim 10^{-4}$s. In these operating conditions, we approach the limits of lateral resolution of the SIMS method, which are set by the size of the collision cascades initiated by the incident ions (Liebl, 1975, 1980). This is accomplished with a 40 keV Ga^+ or In^+ beam from a high resolution scanning ion microprobe developed by the University of Chicago (UC) in

collaboration with Hughes Research Laboratories (HRL). Descriptions of the instrument and preliminary accounts of its performance have been reported previously (Levi-Setti et al., 1984 a,b).

The UC-HRL SIM/SIMS

Optical Column

The schematics of the new microprobe are shown in Fig. 1. The optical column comprises a LMIS enclosed in a Ta housing, placed ~ 1 mm from an extraction aperture, also made of Ta. The optical aperture is placed at the entrance of an asymmetrical triode lens, which operates in the decelerating mode (Orloff and Swanson, 1979). A drift space following this lens is occupied by an octupole deflector, used to center the LMIS tip on the optical axis of the column by viewing the crossover aperture, which also serves the purpose of differential pumping between source and specimen chambers. A dual octupole deflection assembly provides for double deflection of the beam. A final einzel lens focuses the probe on the target. A compendium of operating parameters, referring to the configuration used for highest resolution (thus far), is given in Table 1A. Plots of the theoretical probe diameter d_p (Levi-Setti and Fox 1980 and Levi-Setti et al., 1984b) as a function of the source acceptance half-angle α_0 are shown in Fig. 2 for probe voltages 30 and 50 kV, extraction voltage V_s=10 kV, typical source energy spread (FWHM) 10 eV, for two assumed values of the virtual source size, 10 and 50 nm respectively. For most of the useful range of these curves, the predicted spot size is chromatic-aberration limited. By varying the size of the beam defining aperture (thus far at settings of 25, 12.5 and 5 μm, we have explored the shape and size of the focused probe. From the gaussian profile of grooves sputter-etched in Au-coated wafers, we have determined a d_p FWHM of 90 and 43 nm at α_0 values of 0.78 and 0.39 mr respectively, and a peak source angular intensity of ~ 15 μA/sr (Levi-Setti et al., 1984b). For the smallest α_0 (0.16 mr), determined by a Ta aperture canal 5 μm in diameter, 25 μm long, the probe size was inferred from the observed image resolution, since it has proven difficult to obtain well defined etched grooves in Au. For source currents of 2μA, the probe currents obtained for the three explored settings are 32, 8 and 1.6 pA, consistent with a purely chromatic-aberrated regime, with probe diameter proportional to α_0, and probe current to α_0^2. We have not reached as yet the angular region where the virtual source size may limit the probe size. We can state with some confidence, however, that the virtual source size does not exceed ~ 50 nm. Some difficulties are presented to further our quest for the limiting probe size, which will require the use of aperture ~ 1 μm in diameter with very high aspect ratio. We have witnessed the gradual widening of the laser-drilled 5 μm Ta aperture until almost complete destruction of the 25 μm thick Ta aperture foil, due to sputter erosion, over 3–400 hours of source operation.

Detection, image display and SIMS instrumentation

The ISE and ISI detection scheme adopted for imaging of the surface topography and material contrast in the UC-HRL SIM is based on the experience gained in our studies with the prototype UC-SIM (Levi-Setti, 1983). As shown in Fig. 1, two channel electron multiplier detectors (CEM) overlook the target region at a shallow angle. A summary of ISE and ISI imaging data is given in Table 1B. All micrographs to be shown here were obtained in the "pulse-mode," where individual CEM pulses are

TABLE 1
Specifications of UC-HRL SIM/SIMS at highest explored resolution

A. Optical Column	
–Source extraction voltage	5–20 kV
–Probe voltage	40–60 kV
–Primary ions	Ga^+, In^+ from LMIS
–Primary ion current	1.6 pA
–Probe size (theor.)	20 nm
–Optical aperture size	5 μm, Ta
–Magnification	0.4
–Working distance	2.5 cm
B. Imaging Data, Surface Topography or Material Contrast	
–Signal	ISE or ISI
–Detectors	2 CEM
–Detector bias	+ 300 V, −3000 V
–Best image resolution	20 nm
–Raster size	1024 × 1024 pixels
–Dwell time/pixel	0.5 μs – 16 ms
–Optimal size of imaged area	20 × 20 μm^2
–Imaging modes	pulse or analog
–Typical exposure time	256 sec. for reproduction quality
–Statistics for continuous tone	10 – 25 counts/pixel
C. SIMS Data, Mass Spectra	
–ISI energy window	~ 10 eV
–Target voltage bias	± 100 eV
–Quadrupole voltage offset	± 0 – 10 eV
–CEM collection voltage bias	± 3000 V
–Useful M/ΔM	200 – 1000
–Area scanned	5 × 5 μm
–Depth eroded (S=3, 1.6 pA, 40 keV Ga^+	~ 130 nm/hr
–Atom fraction detected e.g., Ca^{40} in fluoroapatite, S=3)	1/250
–Mass resolved count rates (e.g., Ca^{40} in fluoroapatite)	2 × 10^4 cps/pA
–Dynamic range (1 hr. spectrum)	4 – 5 decades
D. SIMS Data, Isotopic Maps	
–Beam current (40 keV Ga^+ or In^+)	1.6 pA
–Best map resolution	20 nm
–Raster size	1024 × 1024 pixels
–Optimal size of imaged area	20 × 20 μm
–Typical scan time	32 – 512 sec.
–Maximum erosion depth for optimal map (512 sec., S=3)	1.2 nm
–Peak statistics (e.g., Ca^{40} in fluoroapatite)	15 counts/pixel

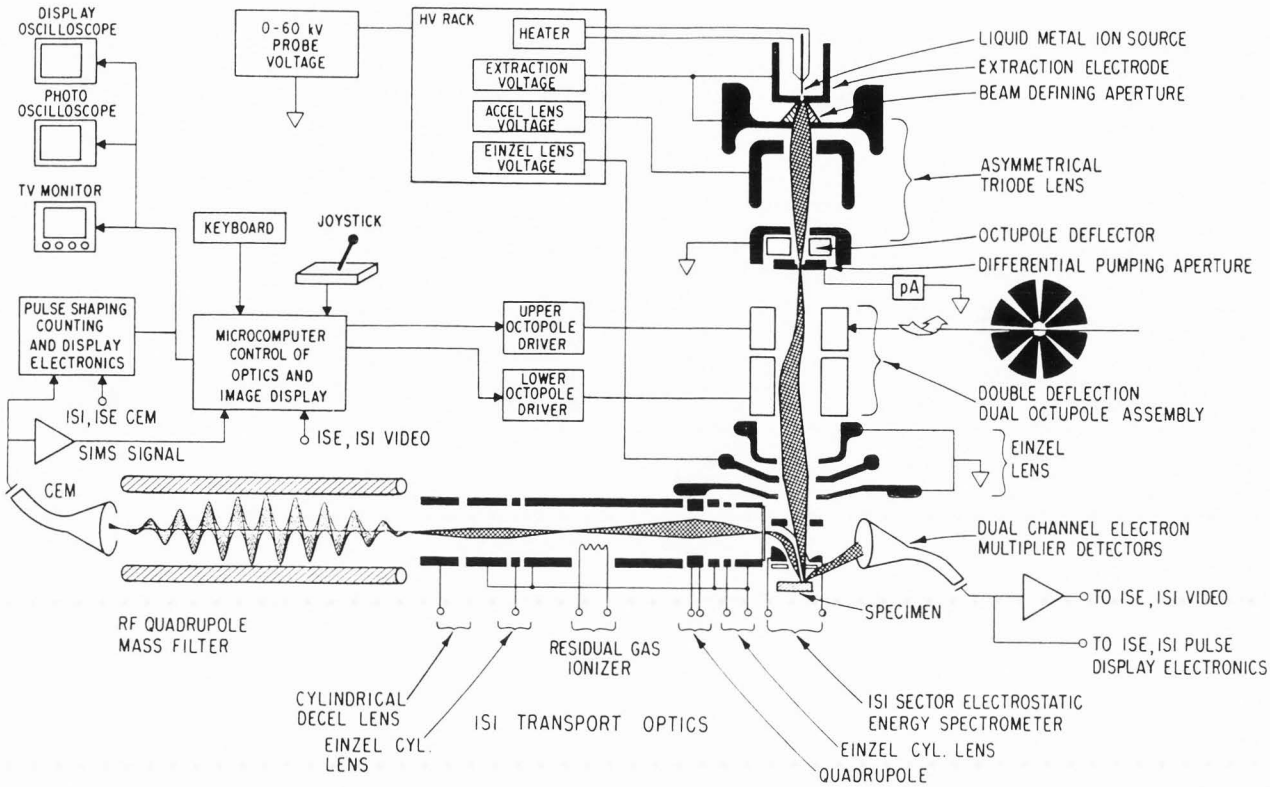

Fig. 1. Schematics of the UC-HRL scanning ion microprobe.

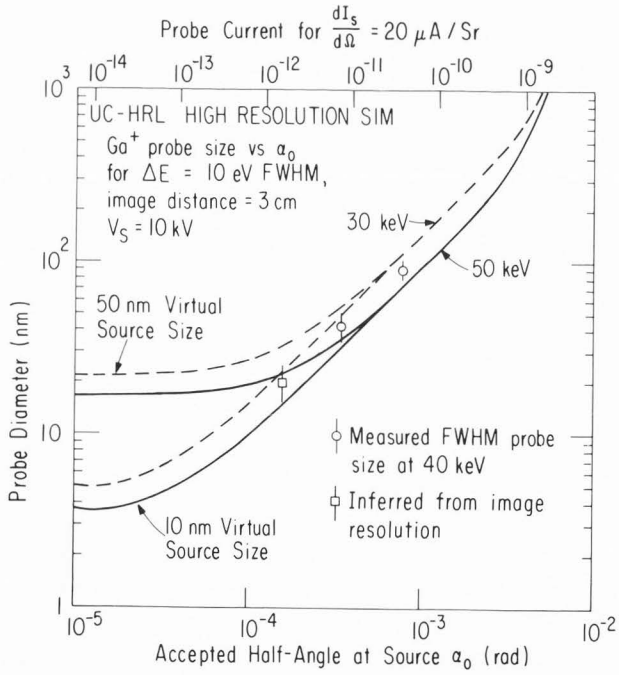

Fig. 2. Calculated probe diameter (d_p) vs beam acceptance half-angle at the source (α_0) for the Ga-probe in the UC-HRL SIM. Experimental points at three beam-defining aperture settings are shown.

discriminated, amplified, shaped and displayed with variable width and amplitude on a high resolution CRT. Images are recorded on 7 ×7 cm^2 Polaroid film in single-pass scans. A Z80-based microprocessor controls the beam deflection system and stigmator. The digital raster can be varied from 16 × 16 to 1024 × 1024 pixels/frame. For reproduction-quality micrographs, including SIMS maps, we use the largest raster size. Raster sizes of 256 or 512 are often used for visual imaging and SIMS spectra acquisition on target areas which would be uniformly sampled with a 1024 raster. In so doing, gaps unpatched by the probe are left between pixels, thus reducing the surface of oxygen depletion which would result from a "carpet sweep." The latter however is the condition chosen for optimal imaging, where the size of the imaged area matches the product 1024 × dp, so that contiguous pixels on the sample are mapped on the CRT.

Special precautions have been taken to construct a highly efficient ISI analysis-transport system (ATS) for SIMS microanalysis while maintaining the probe working distance as short as possible, not to compromise spatial resolution. A scheme conceptually similar to that developed by Wittmaack (1979) has been realized within a depth of 2 cm downstream of the front lens of the probe, and shown in Fig. 1. The positive or secondary ions are extracted from the target region by an accelerating potential of, typically, ∓ 100 V, within a distance of a few mm. They are energy-analyzed by a 90° electrostatic prism and focused onto a slit transmitting ions within an energy window of ± 10 eV. A transport system subsequently focuses the transmitted ions, after deceleration, to the entrance of an RF quadrupole mass filter, so as to match the acceptance requirements of the latter. The center of the quadrupole is maintained at an offset potential of a few volts, relative to the target potential. A potentiometric voltage divider and two 0–300 V power supplies provide

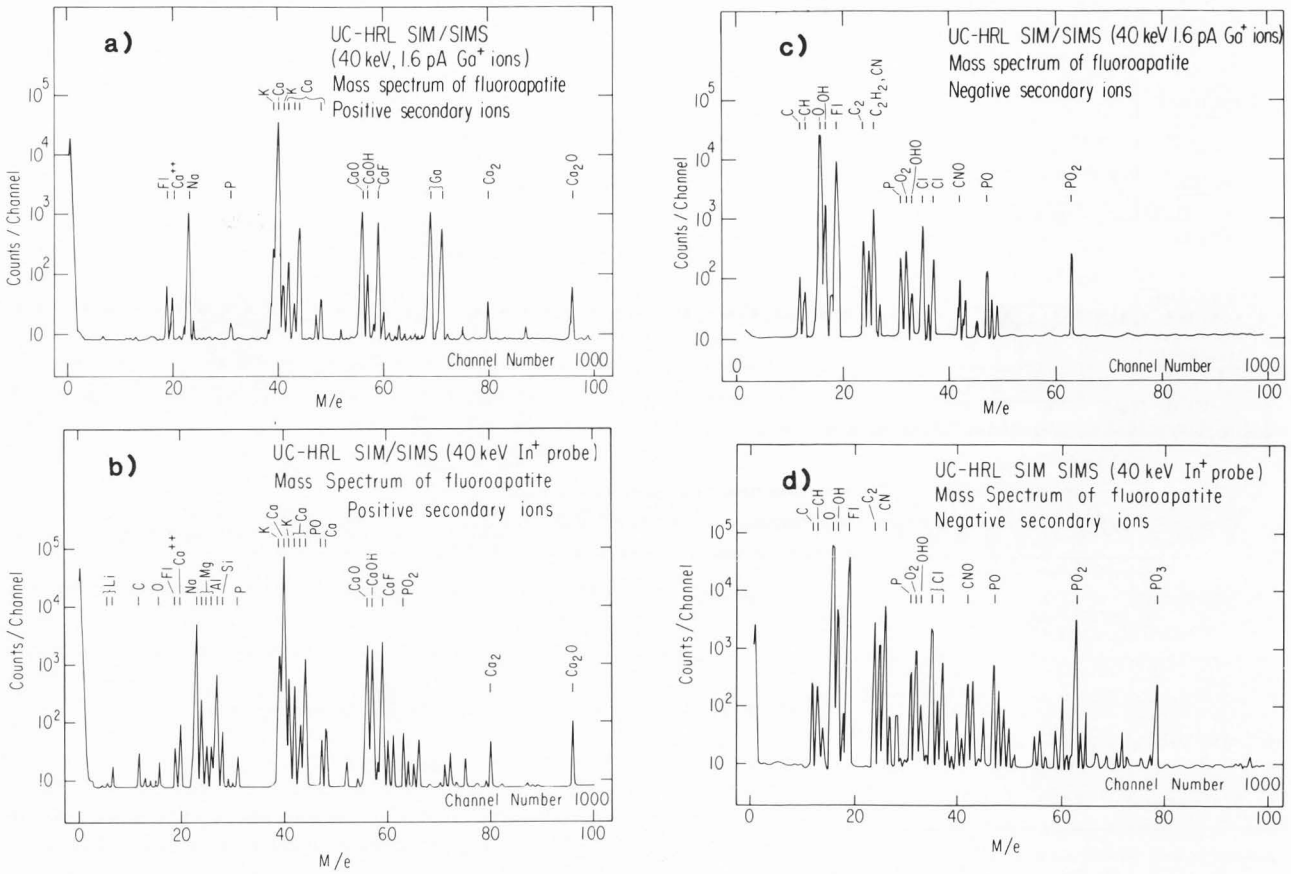

Fig. 3. Comparison of mass spectra obtained for a sample of fluoroapatite. Positive ISI spectra are shown in (a) and (b) for, respectively, a 1.6 pA, 40 keV Ga^+ probe and a 10 pA, 40 keV In^+ probe. The total ion dose was comparable in the two cases. Negative ISI spectra are shown in (c) and (d) for, respectively, the same probes as in (a) and (b). The total Ga^+/In^+ doses in this case were in the ratio of ¼.

for 12 voltages required to operate the complex optics of the ATS. A heated filament within a drift space in the ATS can be used to ionize the residual gas by electron bombardment, for calibration purposes as well as residual gas analysis. The secondary ions transmitted by the quadrupole are accelerated to ± 3000 V for efficient detection by a CEM. The SIMS CEM signal is processed in the same way as the ISE or ISI signals for pulse-mode image display. A scaler gives the total pulse count for every map recorded. Mass spectra are accumulated with a multichannel scaler (MCS) and printed on a chart recorder. A summary of SIMS data, relevant to either mass spectra acquisition or isotopic mapping, is given in Tables 1C and 1D, respectively.

Conditions for High Resolution SIMS Imaging

Several issues regarding high resolution imaging microanalysis have been examined previously (Ruedenauer, 1984; Levi-Setti et al., 1984a). In a digitally controlled raster scan coupled to a SIMS system, there exists a condition on the minimum dwell time t_d per pixel, to preserve synchronous image display without loss of bandwidth. This is due to the non-negligible time of flight, $t_f = \ell(2E/M)^{-½}$ that the ISI of energy E, mass M, take in travelling an overall distance ℓ from the target through the ATS and RF quadrupole. For our system, the condition $t_d > t_f$ implies $t_d > 10^{-5}(M)^{½}$, for M in amu. Thus, a map with 10^6 pixels for e.g., Na^{23} will require a minimum acquisition of ~ 50 s, one for In^{115} ~ 110 s, etc.

In practice, to maintain the statistics of counts/pixel at a meaningful level of signal/noise ratio, it is often desirable to use acquisition times longer than the above minimum. On the other hand, an upper bound on t_d is imposed by the desire to maintain a monolayer O_2 coverage on the sample during a SIMS scan to enhance the ISI yields (Blaise and Bernheim, 1975), thus improving SIMS sensitivity and image statistics. There exist two conditions to satisfy the requirement, depending on whether oxygen replacement is available or not.

No oxygen replacement

ISI yield enhancement is still effective, as long as the original O_2 coverage is not depleted during the SIM scan. For a monolayer O_2 coverage of atomic surface number density n_0 equal to that of sample atoms N_0, assuming equal sputtering yield Y for both species, the original O_2 coverage is not consumed provided $t_d < N_o/J_pY$, where J_p is the probe current density. In our case, J_p is ~ 0.5 A/cm². For Y = 2, t_d ~ 160 μs.

The implication of this upper limit on t_d is that longer dwell times will fail to increase the accumulated statistics in proportion. This however applies to carpet sweep scans, such as those at the optimum magnification (20 × 20 μm² in size

for our smallest spot size). In our experience t_d up to 512 μs have been tolerated in several cases, without serious reduction in the ISI yields. This may indicate the presence of more than one O_2 monolayer on the sample surface. This restriction is also much less stringent or absent when dealing with oxidized or oxygen-rich materials. In addition, when the area scanned is larger than the optimal size, gaps between pixels will be left untouched by the probe in one scan. This will then allow several maps of the same area to be recorded at maximum dwell time per pixel.

With oxygen replacement

In this case, saturated O_2 coverage during the sputtering process is maintained by an ambient pressure $P(O_2)$ such that the rate of oxygen molecule impact on the sample matches their removal rate by sputtering. As discussed elsewhere (Levi-Setti et al., 1984a), we have extended the derivation by Blaise and Bernheim (1975) to our case, where the ion beam dwells for a time t_d over n pixels per frame. The resulting condition is, $P(O_2) \geq N_0 \sigma J_p \; Y \; (2\pi \; mkT)^{-1/2} n^{-1}$, where N_0 = surface atomic density of the solid, σ is the ejection cross section of the adsorbed O_2, Y the sputtering yield of the sample. For J_p = 0.5 A/cm^2, Y = 2, T = 300 °K, n = 10^6 as in our experiment conditions, $P(O_2) \geq 1.8 \times 10^8$ torr. Although facilities for O_2 flooding of the specimen chamber in our microprobe have been recently installed, the results to be presented here still refer to the cases where no external O_2 replacement was available.

SIMS microanalysis with finely focused Ga^+ and In^+ probes

The trade-off between SIMS sensitivity and spatial resolution is a well known issue, discussed in detail in many reviews (see e.g., Liebl, 1975; McHugh, 1975). Extension of these considerations to the range of probe size to be anticipated for LMIS-based instruments have also been presented previously (Levi-Setti and Fox, 1980; Ruedenauer, 1984). In proposing the specific optical column design on which the UC-HRL SIM is based, Levi-Setti and Fox (1980) have anticipated the limiting sensitivity of the instrument for two cases: a sample-volume limited performance, such as relevant in the analysis of particulates, and a sample-volume unlimited performance, relevant in bulk analysis. In essence, these considerations lead to the expectation that only major concentration fractions ($\gtrsim$ 10%) are detectable in micrograins at the 10 nm level, and that ppm concentrations require the consumption of μm-size volumes. These limits refer to the conventional assumption of maximal overall SIMS detection efficiency $\eta\gamma \simeq 10^{-3}$, where η is the collection efficiency, and γ is the ion fraction (McHugh, 1975; Levi-Setti and Fox, 1980). The UC-HRL SIM has met this expectation in some cases, as could be determined with a variety of samples and specifically with a sample of natural fluoroapatite (Iron Mountain, Cerro Mercado, Durango, Mexico) of known composition (Young et al., 1969) with 23% atomic Ca concentration. From an observed counting rate of 2×10^4 cps/pA for Ca^{40+}, assuming a sputtering yield of S = 3 (Lodding, 1983), we obtain an overall detection efficiency of 4×10^{-3}, or 1/250 sputtered ions, as summarized in Table 1C.

Although SIMS mass spectra of apatites have been studied extensively (Lodding et al., 1978) using the Cameca IMS 300 analyzer, and are therefore well known we present in Fig. 3 the spectra for the fluoroapatite sample referred to above for comparison. This is relevant in this context since our microprobe

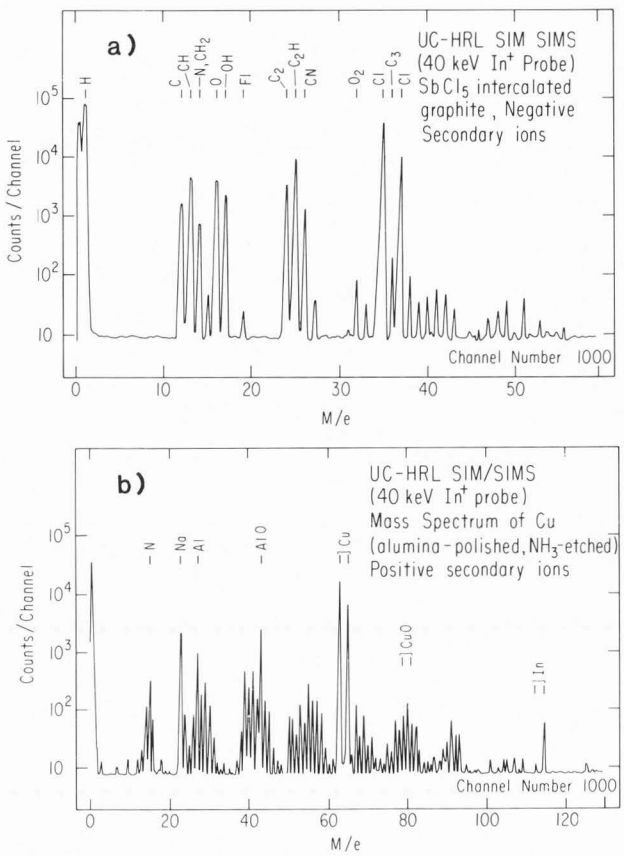

Fig. 4. Mass spectra obtained with a 10 pA, 40 keV In^+ probe. Fig. 4(a) refers to a freshly cleaved sample of $SbCl_5$, stage 4 intercalated, highly oriented pyrolithic graphite. Fig. 4(b) refers to a Cu sample, polished with alumina powder and etched in HNO_3.

is operating in rather unconventional conditions when compared with the current, spot size, incident energy and ion species usually employed in SIMS. The above authors used a 14.5 keV O^- beam for positive ISI, a 5.5 keV O^- for negative ISI, with currents ~ 0.5 μA and beam spot size ~ 60 μm. In Fig. 3(a) and 3(b) we compare positive ISI spectra obtained, respectively, with a 1.6 pA, 20 nm, 40 keV Ga^+ probe and a 10 pA, 50 nm, 40 keV In^+ probe, for a comparable overall ion dose between the two spectra. In Fig. 3(c) and 3(d) we compare negative ISI spectra for the two kinds of probe. However, in the latter case the overall ion dose was ¼ for Ga^+ vs. In^+. The samples were embedded in epoxy, sectioned and lightly coated with Au-Pd to eliminate charging effects. They were analyzed at an ambient pressure of ~ 10^{-8} torr.

The peak counting rate that we observed for Ca^{40} with the Ga^+ probe was 3.2×10^4 cps, corresponding to an uncorrected yield of 2×10^4 cps/pA. Peak counting rates reported by Lodding et al. (1978) for the Cameca IMS 300 are a factor of ~ 10^3 higher than ours, but the corresponding yields are only ~ 10^{-3} of what we observe. Accounting for the much reduced dynamic range in our case (~ 3 decades smaller for positive ISI, ~ 2 decades smaller for negative ISI), the spectra of Fig. 3 are remarkably similar to those of Lodding et al. (1978), (aside from peaks such as C^-, CH^-, C_2^-, C_2H^-, CN^-, CHO, which may be attributed to contamination from the embedding

medium during sample sectioning).

It should be remarked however that the sensitivity limitation in our case is self-imposed, due to the desire to investigate the residual sensitivity at the limits of lateral resolution. With larger beam defining apertures our probe current can be increased by at least a factor of 10^2, and correspondingly, the spectral dynamic range. Concerning the comparison between the Ga^+ and In^+ probes, we note that for positive ISI (Fig. 3(a) and (b)), the somewhat higher yields for In^+ are consistent with the ratio of sputtering yields from In^+ vs. Ga^+, estimated as 1.4 for Ca (Sigmund, 1969). For negative ISI instead (Fig. 3(c) and (d)), we note that the yields for low mass ISI are depressed for In^+ vs. Ga^+, while the reverse seems to occur for the higher mass ISI. Particularly noticeable is the relative intensity of the PO_2^- peak for the two spectra, larger than the factor of 4 dose difference between Fig. 3(d) and 3(c), and the appearance of a PO_3^- peak for the In^+ probe, absent for Ga^+.

In addition to Ca in fluoroapatite, the highest yields for positive ISI, in the 10^4 cps/pA range, have been observed for the other elements of low ionization potential, the alkali in particular, in silicate minerals and glasses. Comparable yields for the negative ISI have been observed for the elements of high electron affinity, the halogens in particular, and oxygen. At the low end of the scale, the yields for e.g. C^- and C_2^- in graphite for the In^+ probe, are $\sim 2 \times 10^2$ cps/pA. This is illustrated by the spectrum of Fig. 4(a) for a $SbCl_5$-intercalated, highly oriented pyrolithic graphite.

Extensive measurements of the ion yields for metals bombarded with 9 keV In^+ ions have been reported by the Vienna group (Gnaser, et al., 1982; Ruedenauer, et al., 1982; Gnaser and Ruedenauer, 1983; Ruedenauer, 1984). Although a systematic investigation of ISI yields from pure metals has not yet been undertaken with our microprobe, we observe consistently very high yields for metals in a variety of matrices. For the Ga^+ probe, for example, Al metallizations of integrated circuits have shown yields in the range 10^3–10^4 cps/pA, Ti and Cu from a superconducting wire matrix $\sim 10^3$cps/pA respectively, and similar yields are observed for Si, without external O_2 enhancement. For our In^+ probe, we report as an example in Fig. 4(b) the positive ISI spectrum obtained for an oxidized Cu sample, which was polished with alumina powder and etched in HNO_3 for crystallographic purposes. The Cu yields in this case is also $\sim 10^3$ cps/pA. The residue of the alumina polishing is detected by the Al and AlO peaks. Various contaminants or impurities seem to have contributed a rich variety of peaks to this spectrum. In general, the ISI yields with our In^+ probe are ~ 3 orders of magnitude higher than those reported by the Vienna group for O_2-enhanced In^+ bombardment. This discrepancy is most likely attributable for the largest part to the difference in SIMS detection efficiencies between the instruments used. A similar comparison is not directly feasible with the data presented by the VG group for a 10 keV Ga^+ probe with O_2 flooding (Bayly, et al., 1983a and b; Waugh, et al., 1984). From the use of 0.1 –3 nA probe currents however by these authors and a comparison of the statistics in corresponding elemental maps, we must surmise an overall SIMS detection efficiency for the VG system $\sim 10^{-2}$ – 10^{-3} that of the UC-HRL SIM.

In summary, Ga^+ and In^+ probes 20 – 50 nm in size, at 40 keV, are quite comparable to O_2^- probes in the relative yields of positive and negative ISI. When coupled to a highly efficient SIMS system, they still provide ~ 4 decades of spectral sensitivity at currents of 1 – 10 pA in acceptable acquisition times (< 1 hr.).

High resolution ISE and ISI imaging

The basic mechanisms of contrast formation in ISE and ISI (mass unresolved) images obtained with a 40 – 60 keV Ga^+ probe have been discussed in detail previously (Levi-Setti, 1983; Levi-Setti, et al., 1983a). Since "topographic" imaging is playing a fundamental role in the optimization of SIM performance and remains the most accessible gauge to estimate the probe size, we present several such images obtained with the UC-HRL SIM. These will illustrate the present limits of SIM lateral resolution.

Figure 5(a) and (b) shows two views of the eye of *Drosophila melanogaster* obtained in the ISE mode with the Ga^+ probe at 1.6 pA. The image resolution, estimated at 20 nm (from other images at high magnification), reveals the corneal nipple array, the antireflection coating of insect eye-lenses (Miller, et al., 1965). At the higher magnification of Fig. 5(b), much of the detail is lost in a second scan of 256 s due to sputter erosion. Under the 10 pA In^+ beam, the lenses collapse rapidly during visual focusing. Figure 5(c) and (d) shows two views of the SiO_2 skeletons of fossil diatoms, also in the ISE mode. These images exhibit a wide range of gray tones and generally give a life-like rendition of lights and shadows.

Figure 6 shows other diatom details, imaged with the ISI signals. In Fig. 6(a) and (b) the sculpturing of the surface is the result of prolonged erosion by the probe. Fig. 6(b) and (d), with a field of view of 5 μm width, begins to show resolution limitations, although part of the rounding-off of sharp edges is always due to erosion.

Figure 7(a) and (b) shows the topography of the HNO_3-etched surface of recrystallized, etched Cu in the ISI mode. In this case, the texture provides an insight into the lattice orientation in twin structures. The second sample, at a lower level of chemical etch, has been used to revisit our previous Ga^+ studies of channelling contrast (Levi-Setti, et al., 1983b), using a 10 pA In^+ probe. Figure 7(c) and (d) shows the same area, imaged in the ISI mode at 11° and 22° probe incidence angle with respect to the sample surface. The critical axial channelling angles for 40 keV In^+ on Cu range between $\sim 5°$ and 10° for different orientations. Characteristic contrast reversals are observed between the two sides for several crystallites. The level of crystallographic contrast is comparable to that we observed previously for a Ga^+ probe. The two views shown actually represent a subset of a larger range of observations made possible by the use of a newly installed rotatable stage. The channelling profiles for individual crystallites can now be measured and the continuous transitions leading to contrast reversals monitored.

SIMS isotopic maps at high lateral and depth resolution

We have explored the SIMS mapping performance of the UC-HRL SIM in a range of interdisciplinary applications. Out of an already overwhelming amount of collected information, we select for the present purposes a few examples apt to illustrate the new insights which an instrument of this kind can contribute.

Surfaces and interfaces

The fact that the probes of smallest spot size (~ 20 nm) are limited by the chromatic aberration to low current values (~ 1 pA) in our SIM system has revealed itself to be an asset in the mapping of monolayer-thick segregates or contaminants

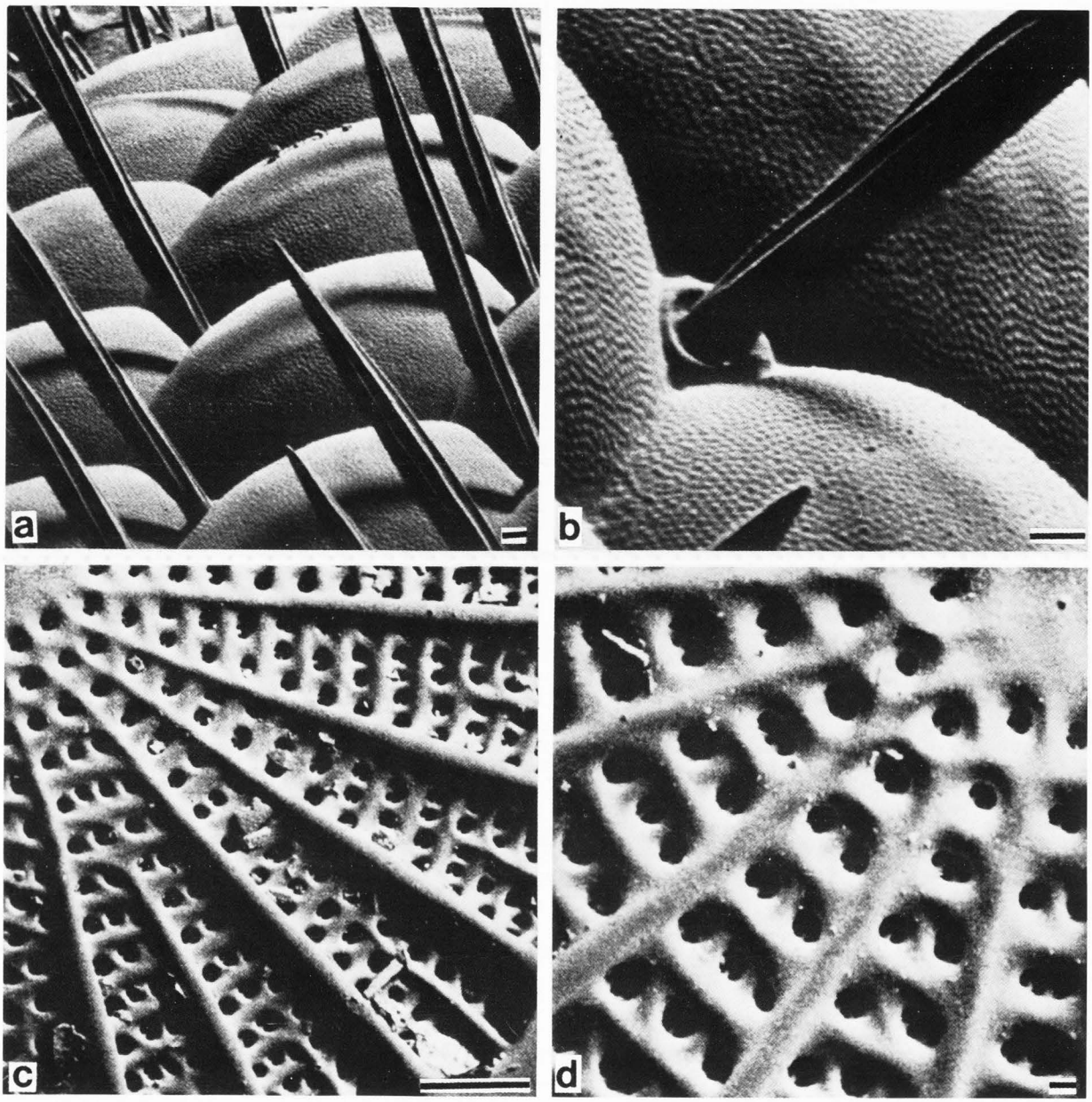

Fig. 5. Topographic contrast in ISE images obtained with a 40 keV, 1.6 pA Ga^+ probe.

(a), (b) Details of the eye of *Drosophila melanogaster*. 256 sec. exposures. Bar = 1 μm.

(c), (d) Fossil diatoms (SiO_2). 256 sec. exposures. Bar (c) = 10 μm, (d) = 1 μm.

on a surface. In fact, since the beam dwell time per pixel cannot be reduced below certain limits, discussed above, to preserve image bandwidth, the probe current must be low enough to ensure sub-monolayer erosion depth per pixel. These conditions are satisfied in our case.

Figure 8(a) is a K^{39+} map of the Au-coated surface of a Si wafer. This map was obtained with an 8 pA Ga^+ beam, ~ 40 nm wide. We are most likely dealing with the residual contamination from a detergent or etchant smear. Similar maps were obtained for Li. The next scan, prior to the disappearance of the surface deposits, was taken for Ga (Fig. 8(b)). Here the incident Ga^+ ions are stopped by the Au layer at a shallow depth and are immediately resputtered. The black dots, corresponding to the islands of contamination, represent most likely areas where the implanted Ga does not reemerge.

Figure 8(c) and (d) shows Cl^{35-} maps of the freshly cleaved surface of highly oriented pyrolithic graphite (HOPG), intercalated with $SbCl_5$ (stage 4). These maps give perhaps the most convincing demonstration of the above considerations concerning surface monolayer imaging. The observed structure can be sharply mapped only in the first scan as shown, for a 1.6 pA Ga^+ probe, while most detail is lost with an 8 pA scan. In a recent interpretation of a large number of similar maps obtained for both stage 2 and stage 4 $SbCl_5$ HOPG (Levi-Setti et al., 1985), the outcome of a collaboration with D.M. Hwang of Bell Communications Research, the bead-like domains are regarded

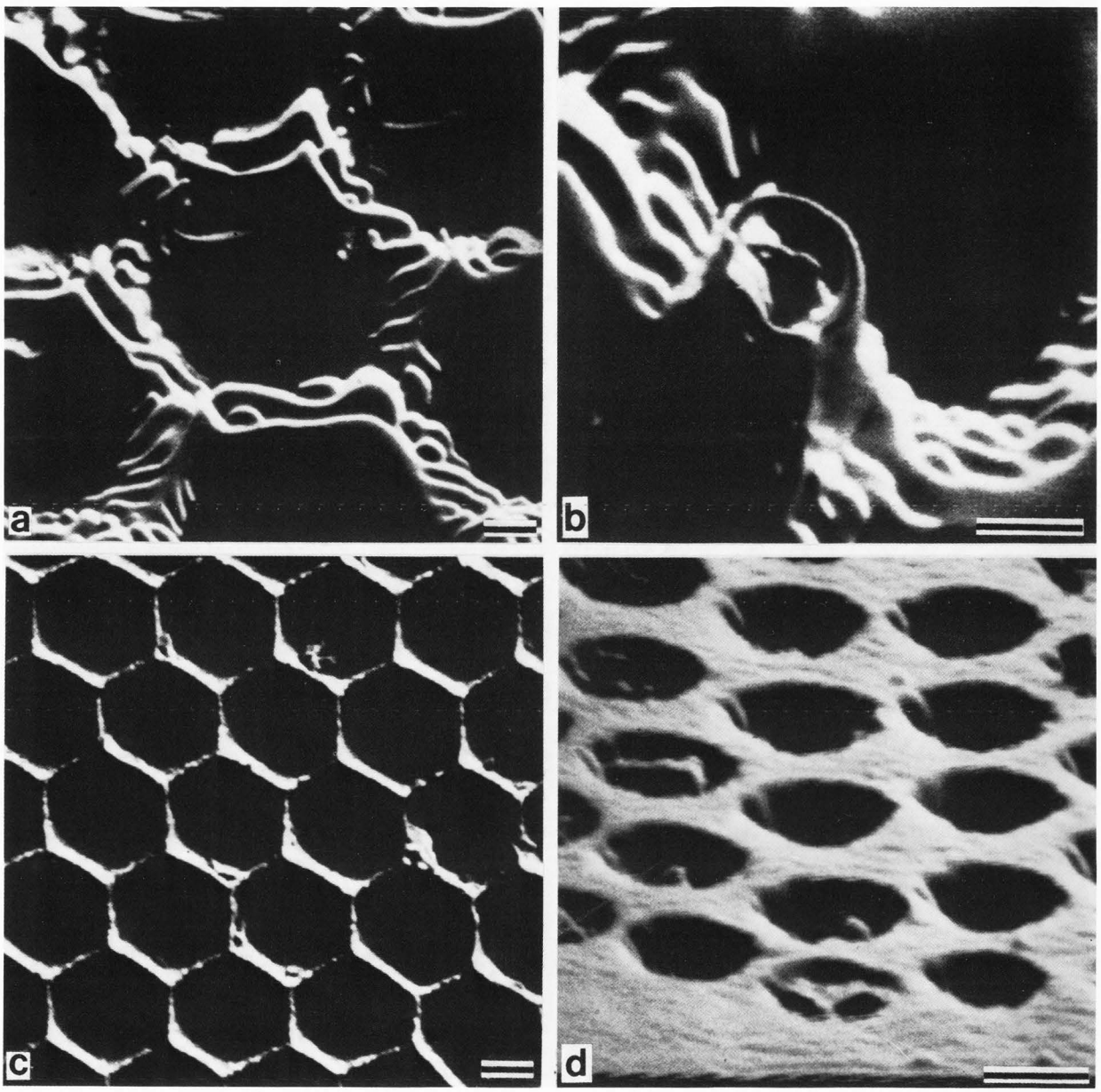

Fig. 6. Topographic contrast in ISI images of fossil diatoms (SiO_2), near the present limits of useful magnification. 1.6 pA, 40 keV Ga^+ probe, 256 sec. exposures. Bars in all images = 1 μm.

as representing the long-sought Daumas-Herold domains (Daumas and Herold, 1969) of graphite intercalation compounds. In freshly cleaved samples most of the exposed domains are expected to evaporate and those we observe are located one monolayer beneath the surface. The line network is attributed to the migration and coalescence of intercalant domains along surface steps and stacking faults. We estimate that, at the magnification of Fig. 8(d), only half a graphite monolayer was sputtered in the scan. Clearly, with a probe consuming several monolayers, the superposition of randomly distributed domains prevents their individual visualization.

Differentiated bulk structures

In collaboration with E. Olsen of the Field Museum of Natural History, we have undertaken to investigate the detailed structure and composition of chondrites, a class of primitive stone meteorites. These consist of aggregates of spherical or ovoidal bodies called chrondules, composed of crystalline silicate minerals (e.g. olivine, pyroxene), cemented together with silicate glass. Of particular interest is the study of the rims exhibited by most chondrules, which were acquired in the environment of the early solar nebula, prior to their accretion into meteorite-sized bodies. Several questions still remain unanswered regarding e.g. the distribution of the volatile elements (e.g. Na, K) within the body of the chondrules, and the possible layering and composition of their rims. An example drawn from this study (Wang et al., 1985) is shown in Fig. 9, where a portion of a chondrule and its rim are shown, as seen through maps for Al^{27+}, Na^{23+},

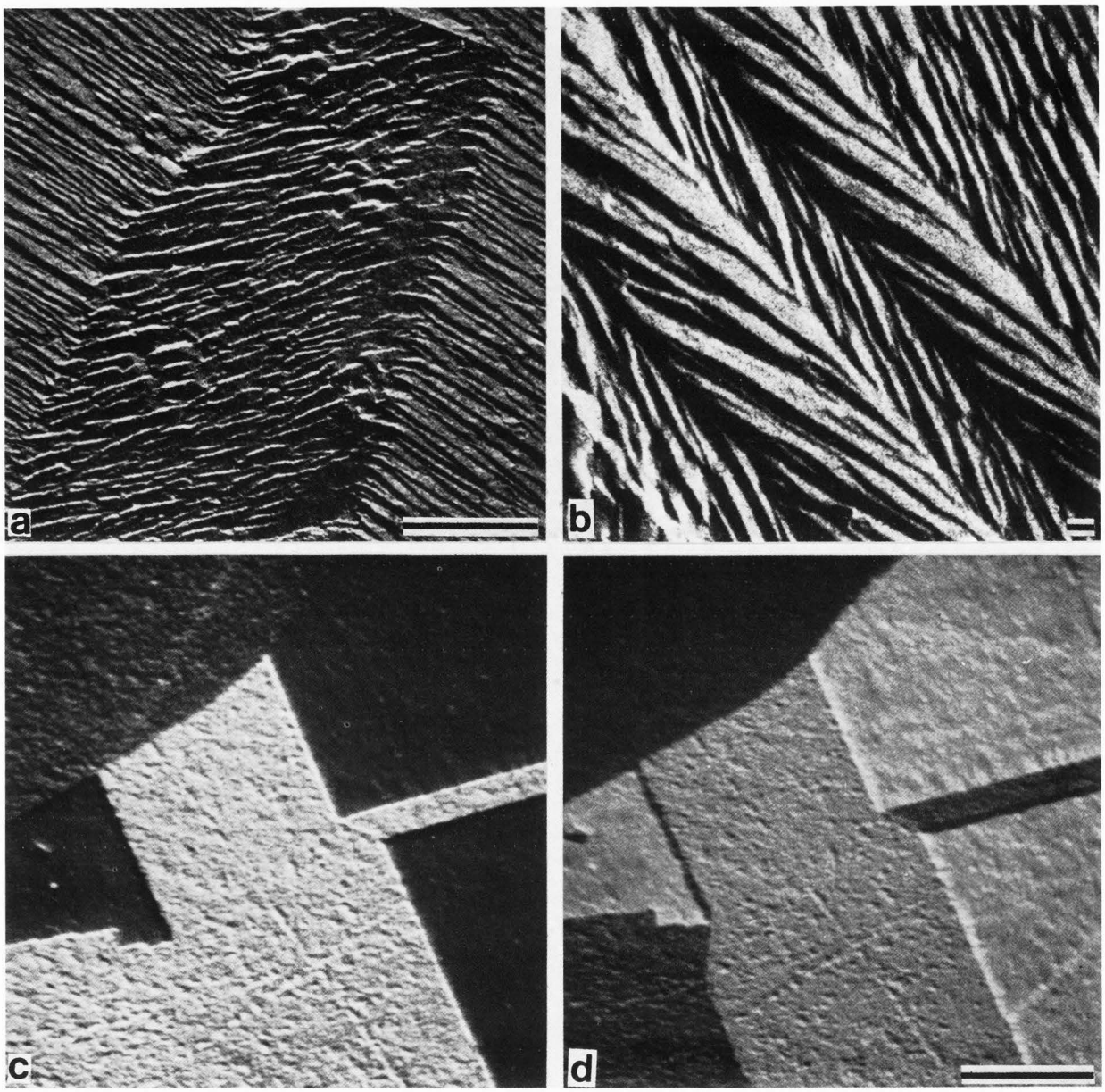

Fig. 7. ISI images of recrystallized, polished HNO_3-etched Cu. 256 sec. exposures.

(a), (b) Surface topography of twin structures, bar = 10 μm (a), 1 μm (b).

(c), (d) Crystallographic contrast with a 10 pA, 40 keV In^+ probe, at 11° primary incidence angle in (c), and 22° in (d). Contrast reversals due to ion-channelling effects. Bar = 10 μm.

Fe^{56+} and O^{16-}, obtained with an 8 pA Ga^+ probe. The sample was a thin section of the Mezo-Madaras meteorite, a type 3 chondrite, polished and lightly coated with Au-Pd. The Fe-rich rim does not show any structure in this case (Fig. 3(c)). Additional maps for the same area, for Mg^{24} and other elements, allow an identification of the mineral phases present. The chondrule (right half of the maps in Fig. 9) appears as an aggregate of olivine grains cemented in a glassy matrix. The olivine grains themselves are rimmed by an Fe-rich layer, a novel feature which may suggest a further primordial stage in the formation of the chondrules themselves. A peculiar feature of the O^- map is represented by the complete absence of an O^- signal from the Fe-rich areas, while O^- is abundantly emitted from the silicate mineral areas.

Studies of biomineralization

For much the same reasons that make them biologically or chemically active, several biologically important elements also have high secondary ion fractions. This is the case most of all for Ca, Na and K. Thus, even at the minimal probe currents of our SIM, mapping of these elements in biological material and biomineralization, is eminently successful. An extensive literature on the subject already exists (see e.g., the reviews by Burns, 1982; Lodding, 1983; Galle et al., 1983). We have ex-

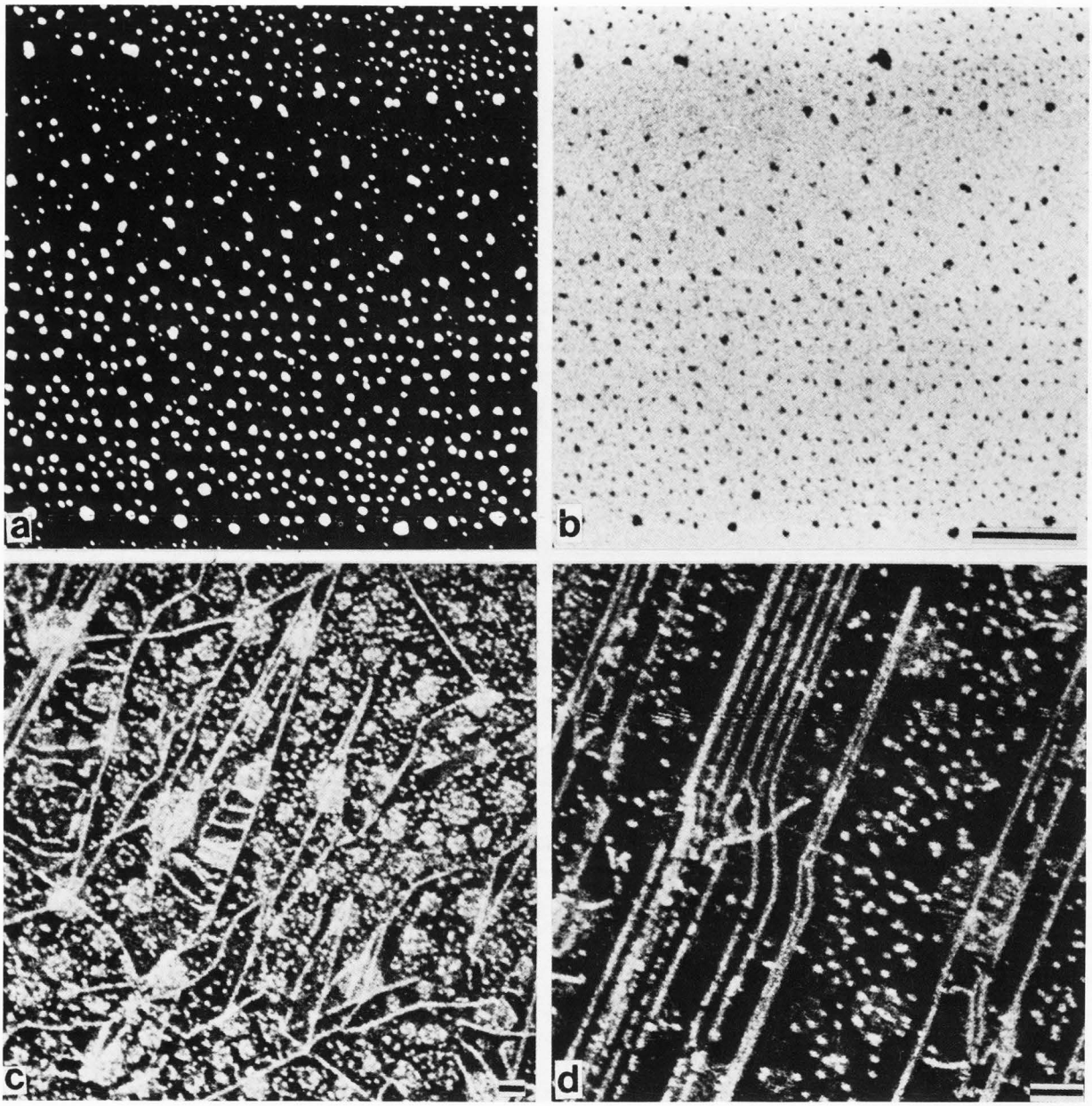

Fig. 8. (a) K^{39+} map of contaminant on Au-coated Si wafer. 8 pA, 40 keV Ga^{+} probe, 512 sec., 5.1 × 10^5 counts.

(b) Ga^{69+} map of same area as in (a). 256 sec., 2.3 × 10^6 counts, bar = 10 μm.

(c) Cl^{35-} map of freshly cleaved, stage 4, $SbCl_5$-intercalated, highly oriented pyrolithic graphite. 1.6 pA, 40 keV Ga^{+} probe. 512 sec., 1.3 × 10^6 counts. Bar = 1 μm.

(d) Same as in (c). 7.2 × 10^5 counts. Bar = 1 μm.

plored applications of our microprobe to studies of human renal calculi and bone of neonatal mice. In the case of renal calculi, the extreme crystallographic contrast in SIM imaging of crystalline materials adds an informative insight. This is shown in Fig. 10(a) and (c), showing images of a fractured surface of a human kidney stone as observed, uncoated, with the ISI signal. The layered structure observed is suggestive of depositional events, much like the "varves" observed in sedimentary deposits at the bottom of tranquil bodies of water, often preserved in shales. The Ca^{40} maps of Fig. 10(b) and (d) show that a radiating structure, perpendicular to the layering is also present. As clearly visible in Fig. 10(d), this structure has a definite lateral periodicity and longitudinal continuity, the latter possibly related to epitaxial crystal growth (Lonsdale, 1968; Deganello and Coe, 1983). We are collaborating with the latter authors in these SIM/SIMS studies. In a further collaboration with D. Bushinsky and F. Coe of the Department of Medicine at UC, studies are in progress on the structure, composition, and growth dynamics of the skull bone (calvaria) of neonatal mice. SIMS imaging microanalysis of such bone in our SIM has revealed that a steep gradient exists in the Ca distribution between surface and interior. While the calvaria surface is covered by a network of organic material extremely rich in Na and K (Bushinsky et al.,

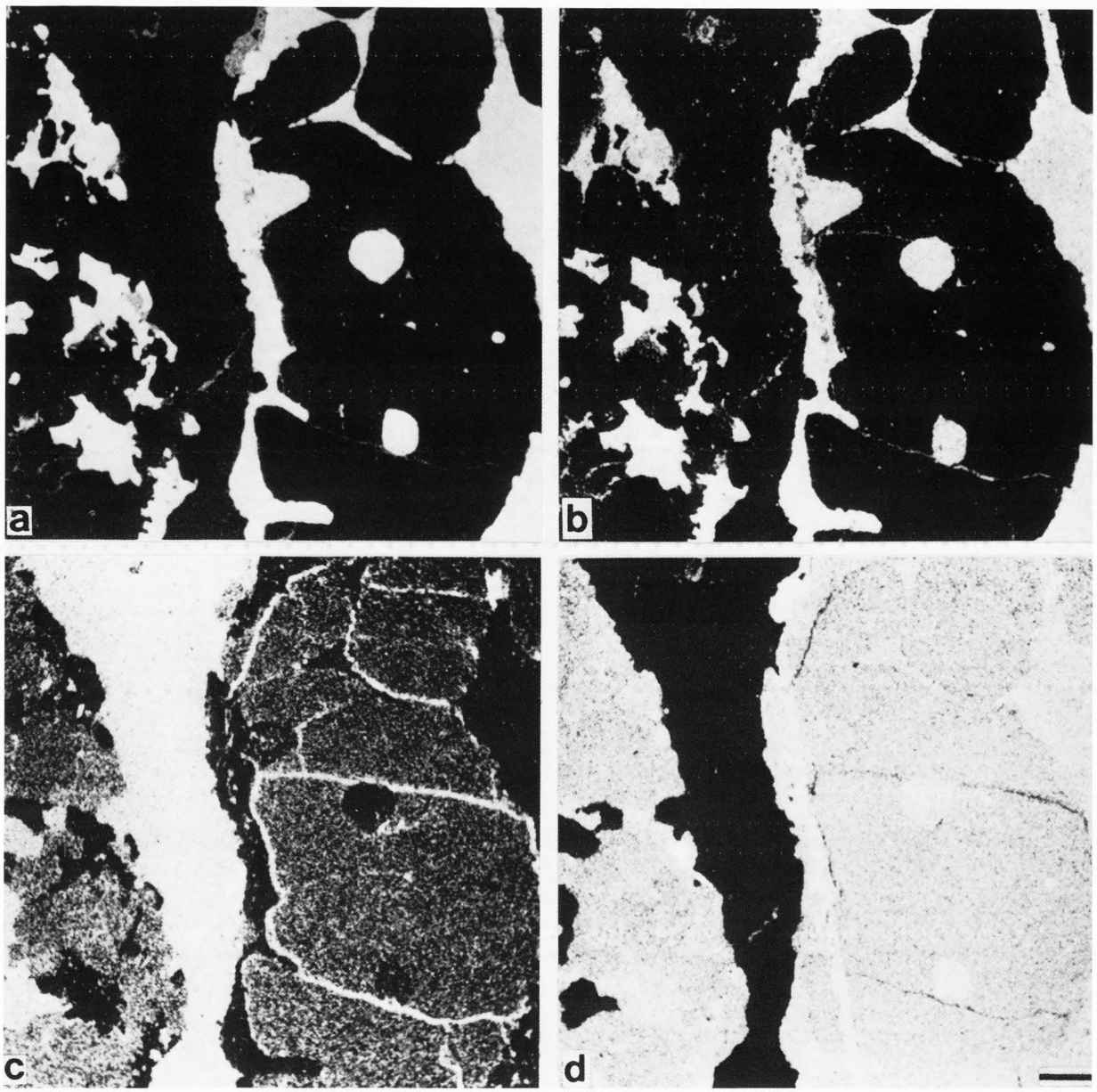

Fig. 9. Elemental maps of polished section of Mezo-Madaras chondrite, 8 pA, 40 keV Ga^+ probe. Bar = 10 μm.
(a) Al^{27+}, 512 sec., 3.0 × 10^5 counts.
(b) Na^{23+}, 256 sec., 1.8 × 10^6 counts.
(c) Fe^{56+}, 512 sec., 4.3 × 10^5 counts.
(d) O^{16-}, 512 sec., 1.2 × 10^6 counts.

1985), only a sparse distribution of Ca nucleation centers is present at the surface, but a much richer Ca distribution, exposed by sputter etching, is present in underlying layers.

Three-dimensional objects

Isotopic maps have been obtained of a variety of samples exhibiting pronounced relief. Since the target is located in a region where the electric field possesses a weak horizontal component (caused by the fringing field of the electrostatic prism analyzer), a certain degree of shadowing does affect the elemental maps of three-dimensional objects. We are dealing then with topographic contrast in SIMS mapping. Several samples of biological objects will illustrate this effect and its extent.

Shown in Fig. 11 (a) and (b) are Na^{23} and Ca^{40} maps of human erythrocytes. A K^{39} map, not shown here, is indistinguishable from that for Na^{23}. The erythrocytes were glutaraldehide-fixed, mounted on a stainless steel support with polylysine, critical-point dried and lightly coated with Au-Pd. Both topographic contrast and edge effects are present in these images, which retain the sculptural appearance of SEM micrographs. Sequential mapping provides information for a full three-dimensional reconstruction of the cells.

Fig. 11 (c) and (d) are Na^{23} maps of the wing of *Drosophila melanogaster*. In Fig. 11 (c), some of the setae remained embedded in the mounting medium. Some are free standing and are seen casting a shadow. This is a high statistics map, showing a richness of gray-level tones. Edge effects are likely to contribute to the extraordinary Na emission from the setae. Intensity

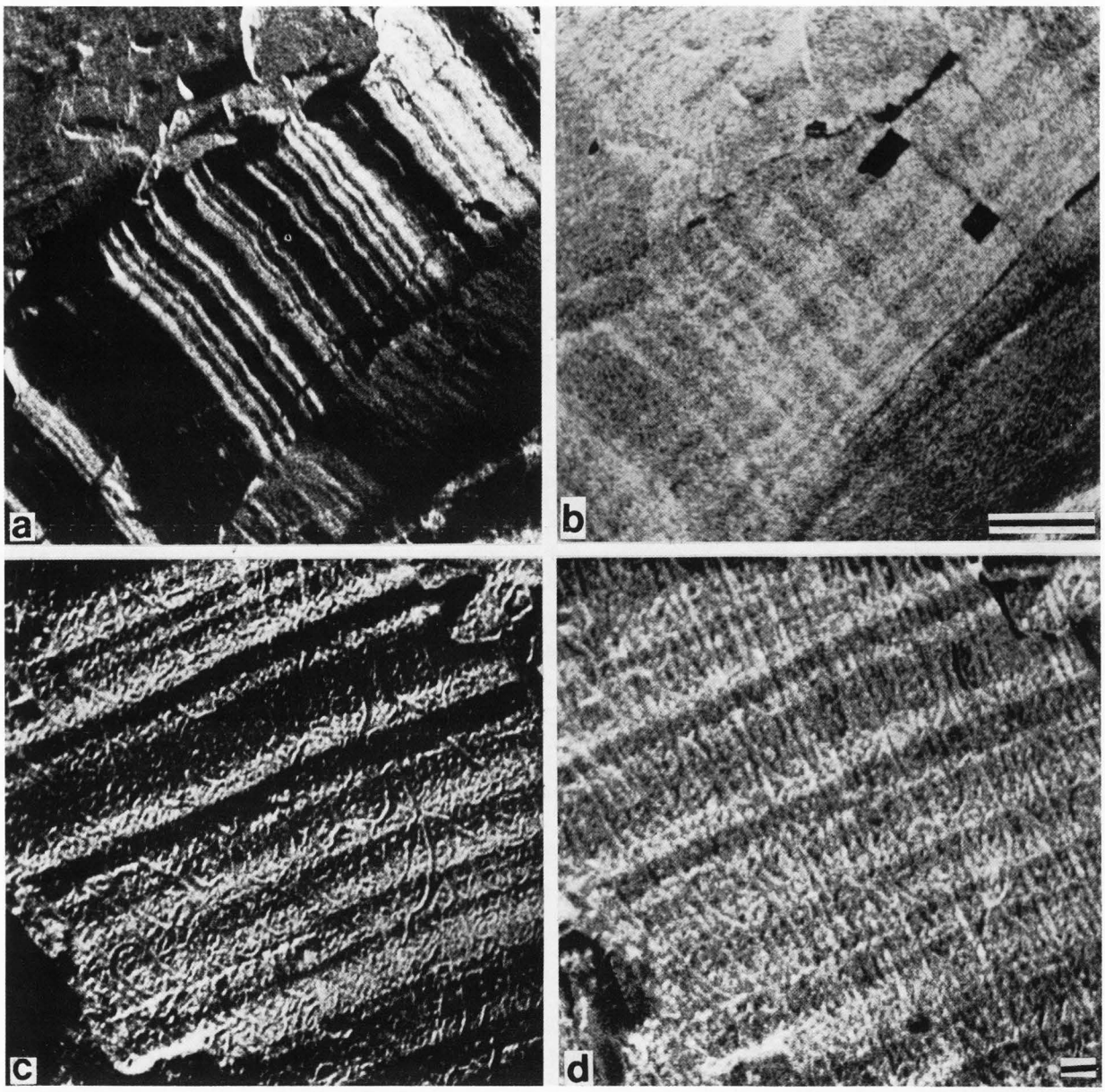

Fig. 10. SIM images of fractured urinary stone. 8 pA, 40 keV Ga^+ probe.

(a) ISI image of uncoated surface.

(b) Ca^{40+} map of area shown in (a). 512 sec., 1.1 × 10^6 counts. Bar in (a) and (b) = 10 μm.

(c) ISI image of uncoated surface, eroded by the ion probe.

(d) Ca^{40+} map of the area shown in (c). 512 sec., 3.5 × 10^6 counts. Bar in (c) and (d) = 1 μm.

discrimination isolates the emission from the protruding setae, as shown in Fig. 11 (d). Similar maps were obtained for K, while the Ca content is minimal.

The ability to perform imaging microanalysis of particulate matter on the surface of free-standing filaments, such as textile fibers, was explored by examining linen fibers from the Shroud of Turin. Samples originally collected by Dr. R. Rogers of Los Alamos National Laboratory, were obtained through courtesy of Dr. J.A. Kohlbeck of Hercules, Inc., Magna, Utah. The samples are in the form of fiber bundles adhering to sticky tape; the entire assembly was given a light Au-Pd coating. SIMS imaging of the fibers showed similarities with the description of ancient, degraded flax fibers (mummy cloth), given by Kleinert (1972). Characteristic is the presence of crumb-like fragments, adhering to the fiber surface, attributed to the residue of epidermal and cortical cells.

Shown in Fig. 12 are elemental maps for Ca^{40}, O^{16}, K^{39} and Cl^{35}. The fiber surface is generally rich in Ca, distributed fairly uniformly with occasional concentration in the crumb-like fragments. The O distribution corresponds rather closely to that of Ca, although more sparse and particulated. Some Cl seems rather uniformly present. K and Na are very abundant in the surface fragments, and occasionally anticorrelate with the Ca content. Some of the alkali-rich fragments also contain some Li, while the Ca-rich particulates also show a signal for mass

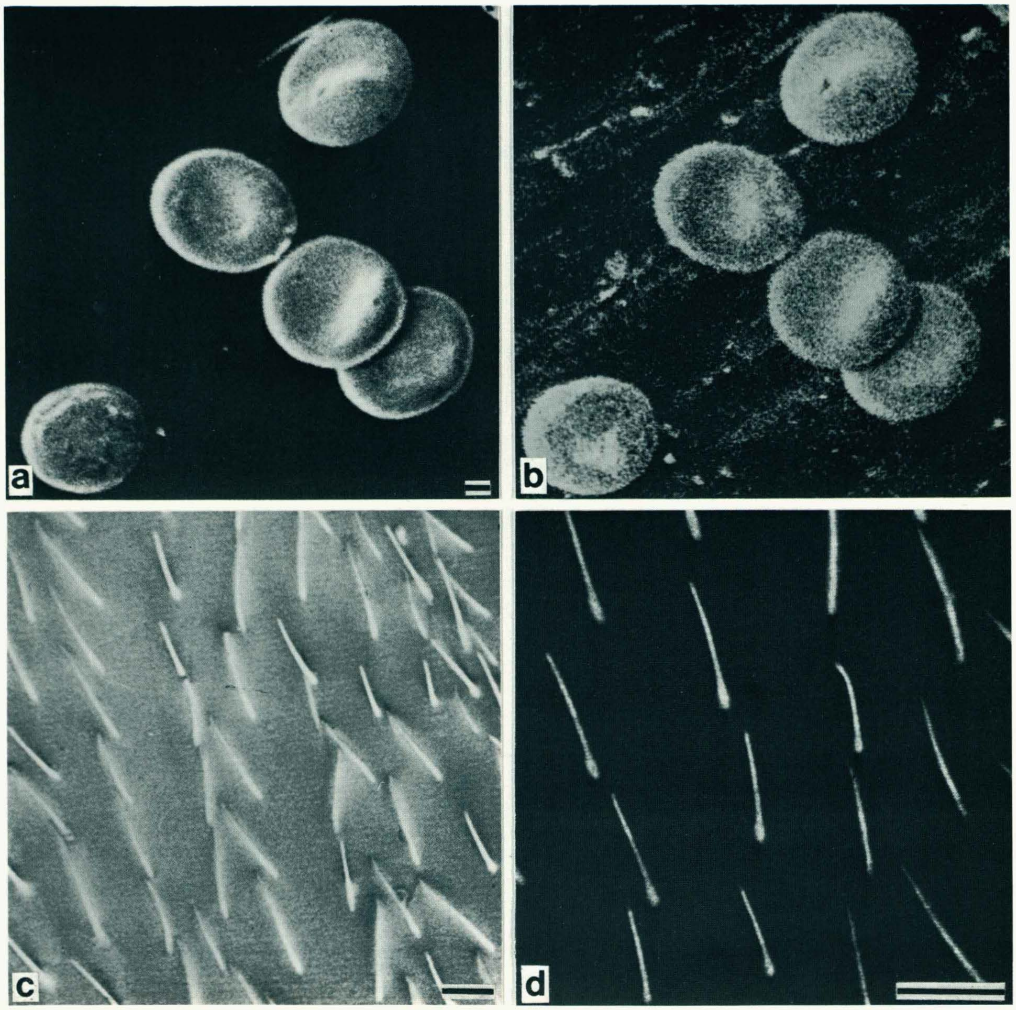

Figure 11. Elemental maps of biological objects with pronounced relief. 20 μA, 40 keV, Ga^+ probe.

(a), (b) Human erythrocytes. (a) Na^{23+}, 128 sec., 1.6 $\times 10^6$ counts; (b) Ca^{40+}, 512 sec., 2.3 $\times 10^5$ counts. Bar = 1 μm.

(c), (d) Wing of *Drosophila melanogaster.*

(c) Na^{23+}, 256 sec., 3.8 $\times$ 10^7 counts; (d) Na^{23+}, 128 sec., 7.7 $\times$ 10^6 counts. Bar = 10 μm.

56, which we cannot separate between Fe and CaO. An unusually high Na content in flax fibers from Egyptian mummy wrappings, when compared to modern linen, had been noted by Kleinert (1972) and attributed to possible residue from incomplete rinsing of the fabric from washing with natural detergents. We will continue this excursion into "forensic archeology" by comparing the Shroud of Turin fibers with those of dated Near Eastern linen, obtained through courtesy of Dr. J.M. Cardamona of Ohio State University.

Stable isotope labelling of biological material

The use of stable isotopes as tracers of biological element transport and metabolism, in conjunction with SIMS imaging microanalysis, has been often advocated (see e.g., Ringo and Krohn, 1978; Burns, 1982). Several promising species which

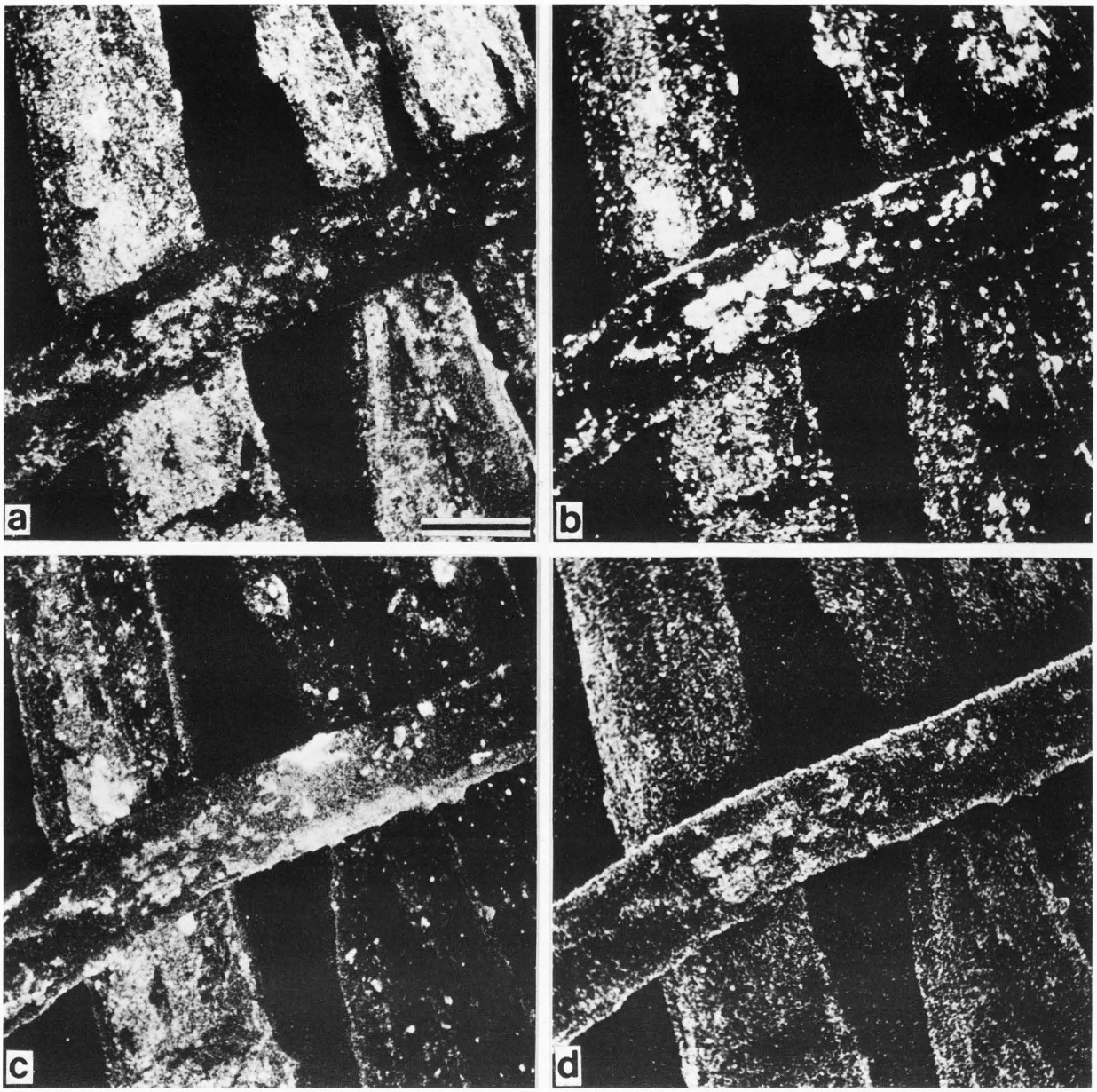

Fig. 12. Elemental maps of linen (flax) fibers from the Shroud of Turin, mounted on sticky tape. 1.6 pA, 40 keV Ga^+ probe. Bar = 10 μm.
(a) Ca^{40+}, 512 sec., 3 × 10^5 counts.
(b) O^{16-}, 512 sec., 1.6 × 10^5 counts.
(c) K^{39+}, 512 sec., 7 × 10^5 counts.
(d) Cl^{35-}, 512 sec., 1.2 × 10^5 counts.

could be used for these purposes are identified in Table 2. They satisfy the basic requirements of such an approach: the element must be biologically active, the natural abundance of the isotope must be small, the element must have high secondary ion yields for SIMS detection, the molecular interferences at the same mass must be absent or small, and last but not least, the isotope must be (relatively) inexpensive.

Ca^{44} is an obvious candidate for the study of the dynamic of Ca fixation in bone. In the extreme case in which bone is modelled by apatite, Table 3 shows what would be the yield of Ca^{44} in a sample examined in the standard mapping conditions for our microprobe, for the natural abundance ratio Ca^{44}/Ca^{40} = 0.0215. The data in the Table indicate that an excess of Ca^{44}/Ca^{40} of ~ 0.01 over the natural abundance would be detectable.

As a compelling extension of the studies mentioned above on the skull bone of the neonatal mouse, we have analyzed samples

which were cultured live, *in vitro*, in a Ca^{44} medium (Bushinsky et al., 1985). Previous determination of the Ca^{44}/Ca^{40} ratio over numerous control samples had shown a ratio consistent with the natural abundances. Surface ratios as high as 0.55 were observed for the Ca^{44}-labeled samples. The active Ca^{44} fixation sites appear to overlap the pre-existing Ca^{40} sites, and visualize the pathways of bone calcification (at least for an *in vitro* culture). Further studies of these growing bones, with *in vivo* Ca^{44} labelling are in progress.

Conclusions

Within the limitations of our initial exploration of high spatial resolution SIMS imaging microanalysis, several novel structural features in a variety of materials have been brought to light which had escaped detection by other microanalytical methods. A combination of factors, including high spatial resolution and low probe intensity, have contributed, at times unexpectedly. One cannot refrain from the overwhelming desire to observe many more old objects with new eyes.

At the same time it is felt that such observations need be accompanied by a new generation of systematic SIMS studies, in which the peculiarities of the interaction and implant of metal ions used as probes may be understood and quantified.

Acknowledgements

We wish to thank Dr. E. Olsen, Dr. S. Deganello, Dr. T. Steck and Drs. R. Rogers and J.A. Kohlbeck for the loans of the Mezo-Madaras meteorite, urinary stone, erythrocyte and Shroud of Turin samples, respectively.

We are indebted to Dr. R.L. Seliger of Hughes Research Laboratories for the loan of several liquid metal ion sources.

This work was supported by the National Science Foundation under Grant No. DMR-8007978, and partially by the NSF Material Research Laboratory at the University of Chicago.

References

Bayly AR, Waugh AR, Anderson K. (1983a). SIMS Microanalysis with a gallium ion microprobe. Nucl. Instr. Methods **218:** 375–382.

Bayly AR, Waugh AR, Anderson K. (1983b). High resolution scanning secondary ion mass spectrometry (SIMS) using liquid metal field ionization sources. In: Scanning Electron Microsc. 1983; I: 23–29.

Blaise G, Bernheim M. (1975). Adsorption of gases studied by secondary ion emission mass spectrometry. Surface Science **47:** 324–343.

Burns MS. (1982). Application of Secondary ion mass spectrometry (SIMS) in biological research: a review. J. Microsc. **127:** 237–258.

Bushinsky D, Levi-Setti R, Lechleider R, Coe F. (1985). High spatial resolution localization of a 44 Calcium label in neonatal mouse calvariae, Abstract submitted to the 7th Ann. Meeting Am. Soc. for Bone and Mineral Research, Washington, D.C., June 15–18, 1985. (Copy available from R. Levi-Setti).

Daumas N, Herold A. (1969). Sur les relations entre la notion de stade et les mécanismes réactionnels dans les composés d'insertion du graphite (On the relations between the notion of stage and the reaction mechanisms in the graphite intercalation compound). C.R. Acad. Sc. Paris **268**:(c-373)– (c-375).

Deganello S, Coe F. (1983). Epitaxy between uric acid and whewellite: experimental verification. N. Jb. Miner Mh. **H6**: 270–276.

Galle P, Berry JP, Escaig F. (1983). Secondary ion mass microanalysis: applications in biology. In: Scanning Electron Microsc. 1983; II: 827–839.

Gnaser H, Ruedenauer FG, Studnicka H, Pollinger P. (1982). Application of a liquid metal ion source in ion microprobe analysis. Proc. 29th Int. Field Emission Symp., H.O. Andren, H. Norden (Eds.), Almqvist Wiksell Int., Stockholm, 401–408.

Gnaser H, Ruedenauer FG. (1983). Positive secondary ion yields under In^+ and O_2^+ bombardment. Int. J. Mass Spectrum. Ion Phys. **46**: 503–506.

Kleinert TN. (1972). Ageing of cellulose. Pt. VI. Natural ageing of linen over long periods of time. Holzforschung, **26**: 46–51.

TABLE 2
Promising Candidates for Stable-isotope Labelling of Biological Material

Isotope	Natural abundance (%)	Ion charge of preferred labels
Mg^{24}	78.99	
Mg^{25}	10.00	← +
Mg^{26}	11.01	← +
S^{32}	95.02	
S^{33}	0.75	← –
S^{34}	4.21	← –
K^{39}	93.26	
K^{41}	6.73	← +
Ca^{40}	96.94	
Ca^{42}	0.65	← +
Ca^{44}	2.086	← + ***
Fe^{54}	5.8	← +
Fe^{56}	91.72	

TABLE 3
Sensitivity in Optimal Mass-resolved Imaging
UC-HRL SIM/SIMS – 512 sec. Exposure

Spot size	20 nm
Beam current	1.6 pA
Field of view (side)	20 μm
Area	$4 \times 10^{-6} cm^2$
Depth sputtered (S=3)	5×10^{-13} cm^3
Atoms in volume	1.5×10^{10}
Ca^{40} atoms in volume (apatite)	3.4×10^{9}
Ca^{40} ions detected (exp.)	1.5×10^{7}
Ca^{44} atoms in volume	7.5×10^{7}
Ca^{44} atoms detected	3.3×10^{5}
Min. detectable Ca^{44} excess over natural abundance (3σ)	6×10^{-3}
Counts for 1 ppm Ca in volume	66

Levi-Setti R. (1983). Secondary electron and ion imaging in scanning ion microscopy. In: Scanning Electron Microsc. 1983; I: 1-22.

Levi-Setti R, Fox TR. (1980). High resolution scanning ion probes: application to physics and biology. Nuclear Inst. Methods **168:** 139-149.

Levi-Setti R, La Marche PH, Lam K, Shields TH, Wang YL. (1983a). Secondary ion imaging in the scanning ion microscope. Nucl. Instr. Methods in Phys. Res. **218:** 368-374.

Levi-Setti R, Fox TR, Lam K. (1983b). Ion channelling effects in scanning ion microscopy with a 60 keV Ga^+ probe. Nucl. Instr. Methods **205:** 299-309.

Levi-Setti R, Wang YL, Crow G. (1984a). High spatial resolution SIMS with the UC-HRL scanning ion microprobe. J. Physique **45:** (C9-197)-(C9-205).

Levi-Setti R, La Marche PH, Lam K, Wang YL. (1984b). Initial operation of a new high-resolution scanning ion microscope. SPIE **471:** 75-82.

Levi-Setti R, Crow G, Wang YL, Parker W, Mittleman R, Hwang DM. (1985). High resolution scanning ion microprobe study of graphite and its intercalation compounds. Bull. Am. Phys. Soc. **30:** 240.

Liebl H. (1975). Ion probe microanalysis. J. Phys. **E8:** 797-808.

Liebl H. (1980). SIMS instrumentation and imaging techniques. Scanning **3:** 79-89.

Lodding A. (1983). Quantitative ion probe microanalysis of biological mineralized tissues. In: Scanning Electron Microsc. 1983; III: 1229-1242.

Lodding A, Larsson SJ, Odelius H. (1978). Secondary ion mass spectra of apatites. Z. Naturforsch. **33a:** 697-708.

Lonsdale K. (1968). Epitaxy as a growth factor in urinary calculi and gallstones. Nature **217:** 56-58.

McHugh JA. (1975). Secondary ion mass spectrometry. In: Methods of Surface Analysis, AW Czanderna (Ed.), Elsevier, North Holland, N.Y., 273-278.

Miller WH, Moeller AR, Bernhard CG. (1965). The corneal nipple array. In: The Functional Organization of the Compound Eye, CG Bernhard (Ed.), Pergamon Press, N.Y., 21-33.

Orloff J, Swanson LW. (1979). A Study of some electrostatic lenses for field emission. In: Scanning Electron Microsc. 1979; I: 39-44.

Ringo GR, Krohn VE. (1978). Possible applications of a high brightness gallium source to ion microprobes. Nucl. Instr. Methods **149:** 735-737.

Ruedenauer FG. (1984). Liquid metal sources for scanning SIMS. In: Secondary Ion Mass Spectrometry SIMS IV, A Benninghoven, J Okano, R Shimizu, HW Werner (Eds.), Springer-Verlag, N.Y., 133-137.

Ruedenauer FG, Pollinger P, Studnicka H, Gnaser H, Steiger W, Higatsberger MJ. (1982). First results on a scanning ion microprobe equipped with an EHD-type Indium primary ion source, in: Secondary Ion Mass Spectrometry, SIMS III, A. Benninghoven, J. Okano, R. Shimizu, H.W. Werner (Eds.), Springer-Verlag, NY, 43-48.

Sigmund P. (1969). Theory of Sputtering. I. Sputtering yields of amorphous and polycrystalline targets, Phys. Rev. **184:** 383-416.

Wang YL, Crow G, Levi-Setti R. (1985). High lateral resolution SIMS mapping of meteorite chondrule, Nucl. Instr. Methods in Physics Res., in press.

Waugh AR, Bayly AR, Anderson K. (1984). The application of liquid metal ion sources to SIMS, Vacuum **34:** 103-106.

Wittmaack K. (1979). Secondary ion mass spectrometry as a means of surface analysis, Surface Science **89:** 668-700.

Young ES, Myers AT, Munson EL, Conklin NM. (1969). Mineralogy and geochemistry of fluoroapatite from Cerro de Mercado, Durango, Mexico, U.S. Geol. Survey Prof. Paper 650-D, D84-D93.

Discussion with Reviewers

N.S. McIntyre: Could you please provide details on any procedures that were taken to counteract charging for the specimens analyzed?

Authors: Insulators were coated with a thin film ($\sim$ 5 nm) of Au-Pd in a sputter-coater. This film is rapidly sputtered away from the surface area being scanned in the SIM. Exposure of the insulator, as long as the window thus opened is surrounded by a grounded conducting film, does not affect SIMS operation. The metal ion implant seems effective in making the insulator surface conductive enough to prevent charging. Some recoil implantation of the surface coating is observed, not serious enough, however, to interfere with the mapping or spectra acquisition of the other elements.

N.S. McIntyre: Do you feel that topographic and elemental detail could be separated by using the Ga^+ or In^+ signal as a reference?

Authors: This seems a promising approach, restricted however, to those matrices which are effective in stopping the Ga^+ or In^+ implanted ions close to the surface. The equilibrium concentration of the latter, which depends on the implant rate relative to the sputtering rate, is in fact a function of the range of the probe ions in the target and its sputtering yield (Gnaser et al., 1982).

N. Winograd: What are the prospects of imaging molecular cluster ions? Would this provide any new information?

Authors: Imaging can be performed with any ion species contributing a distinguishable peak in the mass spectrum. Maps have been obtained for e.g. Ga_2^{138+} resputtered from Au surface, $CaOH^+$ in urinary stones (presumably from calcium oxalate), CaO^+ in calcium carbonate, CN^- in organic material, etc. In the latter case, the CN molecule acts as a high sensitivity tracer of N, of lesser ion fraction. Often the hydrides and dimers have a higher ion yield than the parent atoms, as in the case of e.g. CH^-, C_2^-, O_2^-, etc. The mapping of molecular cluster ions can then be performed with better statistics than that of component monoatomic species, when these are difficult to ionize. Furthermore, mapping with distinctive molecular fragments can provide a certain amount of chemical information absent in monoatomic maps.

A. Lodding: Your transmitted secondary ion yields, as shown in connection with the apatite spectra, are indeed impressive. However, your comparison with the yields of "conventional" SIMS applies to circumstances as they were ca 7 years ago. The transmissivity of the "second generation" Cameca equipment is probably still lower than that quoted (N.B. at considerably lower total ion currents) for your instrument, but not by more than one order of magnitude.

G. Blaise: The mass-resolved secondary ion yield which you quote (2×10^4 cps/pA for Ca in apatite) relative to the primary current, is significant in your case since the ions that you collect have been produced by the total probe current. On the contrary, in the case of the probe of the Cameca IMS 300, the primary spot (~ 1 mm^2), is much larger than the imaged field of view (~ 0.05 mm^2), so that only a small fraction (1/20) of the primary current is actually useful in the production of the detected secondary ions. I feel that a comparison between the detection efficiencies of the two instruments in question should take this point into account to be meaningful.

Authors: We appreciate the comment made by A. Lodding concerning the performance of the new vs. the old Cameca equipment. In the context of comparing the yields of our scanning probe vs. those of a direct imaging instrument as the Cameca, the remark by G. Blaise is most relevant. We concur with the notion that a comparison of detection efficiencies should take into account the fraction of the primary beam actually contributing to the detected signal. In terms of economy of sample consumption, however, there remains the fact that in direct imaging instruments, a large fraction of the sputtered ions is not utilized.

G. Blaise: After further investigation, it appears that the primary ion current (0.5 μA, Lodding et al., 1978) used in your estimate of the sensitivity of the Cameca analyser, is in error. In a more recent paper, Lodding and Odelius, (1984) give more realistic values of the current: O^- ions of 15 keV; total current 150 nA; current on an image field of 60 μm in dia.; 15 nA. Another point that must be taken into consideration, when dealing with insulators, as minerals are, is the charging effect. With an O^- probe, it is not possible to compensate for the negative charging of the surface using an electron beam. As a result of consultation with several colleagues involved in the microanalysis of minerals, I propose the following:

Levi-Setti's microprobe:
sample: apatite
element Ca – atomic concentration 0.23
Ga^+ ion – 40 keV
probe current: 1.6 pA
Ca^+ signal: $3.2\cdot 10^4$ cps
yield $Y^+_{Ca\ 0.23} \sim 2\cdot10^4$ cps/pA.

Cameca analyser – Lodding and Odelius, 1984
sample: apatite
element Ca – atomic concentration 0.23
O^- ions – 15 keV (probably charging up effect)
total current: 150 nA.
useful current on 60 μm image field = 15 nA
Ca^+ signal: $3\cdot10^7$ cps
yield: $Y^+_{Ca\ 0.23} \sim 2000$ cps/pA

Cameca IMS 300 (Orsay group)
sample: feldspar
O_2^+ ions – 5.5 keV no charging up effect
Primary current density: 0.16 μA/mm^2
Useful current on 60 μm image field: 0.5 nA.
element Si
atomic concentration: 0.12
Si^+ signal = $2\cdot10^6$ cps
yield $Y^+_{Si\ 0.12} \sim 4000$ cps/pA
element Ca
atomic concentration: 0.04
Ca^+ signal $\sim 6\cdot10^6$ cps
yield $Y^+_{Ca\ 0.04} \sim 1.2\cdot10^4$ cps/pA

Comparing now all the yields for the same atomic concentration of 0.23 one obtains:

Levi-Setti's microprobe – for Ca –	20,000 cps/pA
Cameca (Lodding) – for Ca –	2,000 cps/pA
Orsay group – for Ca –	60,000 cps/pA
Orsay group – for Si –	8,000 cps/pA

This comparison shows the sensitivity is of the same order of magnitude for the two types of instruments in so far as the experimental conditions are rather different (for example the sputtering yield for Ga^+ ions of 40 keV is at least a factor of four higher than using light ions as O^- or O_2^+ of lower energy).

Authors: We very much appreciate the above detailed discussion by G. Blaise regarding the comparison of the sensitivities of our microprobe with that of the Cameca analyser.

G. Blaise: You estimate a ratio of 1.4 for the yields from In^+ vs. Ga^+ probes for pure Ca in fluoroapatite. In your case the problem is to compare the sputtering yield of the fluoroapatite bombarded by In^+, Ga^+ respectively. I have calculated this ratio and found a value of 1.75.

Authors: Thank you for your useful comment.

A. Lodding: Does your present equipment contain any facility for an offset in sample voltage, to minimize molecular peaks and to position the energy pass window at a given range on the secondary ion energy distribution?

Authors: Yes, both sample and quadrupole bias potentials can be varied independently, as well as the width of the energy pass window (in the range 0.5–10 eV). We normally position the energy pass window to bracket the peak of the ISI energy distribution by varying the sample potential relative to the energy analyzer potentials (sample offset). Another offset voltage, between the sample and quadrupole bias potentials (quadrupole offset) determines the velocity of the ISI's through the quadrupole mass filter. Both the mass resolution and the transmission of the quadrupole are affected by this offset, which we maintain in the 0–10 eV range. These aspects of SIMS using quadrupole mass filters are discussed in detail by Wittmaack (1982).

A. Lodding: In connection with your apatite example you have pointed out that, in the negative spectra, the high mass peaks are relatively depressed when Ga^+ primary ions are used, but relatively enhanced by the use of In^+. For example, in the spectrum obtained with Ga^+, the PO_3^- peak is nearly absent. Could this not be due to the well known effect of discrimination against polyatomic ions by "energy offset"? If the impinging

primary ions cause a build-up of charge on the insulating specimen, the energy distribution of the secondary ions is likely to drift past the 10 eV energy pass window of your collector (cf. e.g. the paper by Odelius et al., 1985 in these volumes). Could the observed differences between the spectra obtained with Ga^+ and In^+, respectively, be connected with a difference in the degree of surface "metallization" achieved?

Authors: The same Pd-Au-coated sample was used for both Ga^+ and In^+ mass spectra. Also the SIMS operating parameters were the same in both cases. We can therefore exclude the effects due to an extraneously imposed energy offset. There remains the possibility that local fields, created on the insulator surface within the window opened by the scan on the Pd-Au coating, may be different for the Ga^+ vs. the In^+ implants. The surface resistivity of the implant "metallization" will differ in the two cases, due to the difference in range and sputtering yield for the two species. It is conceivable that different equilibrium surface potentials may be reached on the areas being analyzed, which will also depend on the probe current. Unfortunately this hypothesis is beyond verification for the time being.

Additional References

Lodding A, Odelius H. (1984). Sensitivity and quantitation of SIMS as applied to biomineralization, in: Secondary Ion Mass Spectrometry SIMS IV, A Benninghoven, J Okano, R. Shimizu, HW Werner (Eds.), Springer-Verlag, N.Y., 478–484.

Odelius H, Lodding A, Werme L, Clark D. (1985). Secondary Ion Mass Spectrometry of Glasses: Aspects of Quantification. Scanning Electron Microsc. 1985; in press.

Wittmaack K. (1982). Design and Performance of Quadrupole-based SIMS instruments: A Critical Review. Vacuum **32:** 65–89.

Authors Late Addition: Since this paper was written we have been advised of two additional papers related to the discussion of SIMS sensitivity and spatial resolution:

Slodzian G. (1975). Some problems encountered in secondary ion emission applied to elementary analysis, Surface Science **48**: 161.

Slodzian G, Figueras A. (1980) in Proc. 8th Int. Conf. on X-Ray and Microanalysis, Boston (1977), Pendell Publishing Co., MI, 659–665.